The Astrophysical Journal, 893:129 (12pp), 2020 April 20 https://doi.org/10.3847/1538-4357/ab8017

Neutron Star Radius-to-mass Ratio from Partial Accretion Disk Occultation as Measured through Fe Kα Line Profiles

Riccardo La Placa[1,2,3], Luigi Stella[2], Alessandro Papitto[2], Pavel Bakala[3,4], Tiziana Di Salvo[5], Maurizio Falanga[6,7], Vittorio De Falco[3], and Alessandra De Rosa[8]
[1] Department of Physics G. Marconi, University of Rome "La Sapienza," Italy; riccardo.laplaca@inaf.it
[2] INAF—Astronomical Observatory of Rome, Monte Porzio Catone (Roma), Italy
[3] Research Centre for Computational Physics and Data Processing, Silesian University in Opava, Czech Republic
[4] M.R. Štefánik Observatory and Planetarium, Hlohovec, Slovak Republic
[5] Università degli Studi di Palermo, Dipartimento di Fisica e Chimica, Palermo, Italy
[6] International Space Science Institute (ISSI), Bern, Switzerland
[7] International Space Science Institute Beijing, People's Republic of China
[8] INAF/Istituto di Astrofisica e Planetologia Spaziali, Roma, Italy
Received 2019 December 13; revised 2020 March 4; accepted 2020 March 14; published 2020 April 23

Abstract

We present a new method to measure the radius-to-mass ratio (R/M) of weakly magnetic, disk-accreting neutron stars by exploiting the occultation of parts of the inner disk by the star itself. This occultation imprints characteristic features on the X-ray line profile that are unique and are expected to be present in low-mass X-ray binary systems seen under inclinations higher than $\sim$65°. We analyze a Nuclear Spectroscopic Telescope Array observation of a good candidate system, 4U 1636-53, and find that X-ray spectra from current instrumentation are unlikely to single out the occultation features owing to insufficient signal-to-noise. Based on an extensive set of simulations we show that large-area X-ray detectors of the future generation could measure R/M to $\sim 2 \div 3\%$ precision over a range of inclinations. Such is the precision in radius determination required to derive tight constraints on the equation of state of ultradense matter and it represents the goal that other methods also aim to achieve in the future.

Unified Astronomy Thesaurus concepts: Neutron stars (1108); Low-mass X-ray binary stars (939); Stellar accretion disks (1579); General relativity (641); X-ray sources (1822)

1. Introduction

The central regions of neutron stars (NSs) attain densities close to or exceeding those of atomic nuclei. They provide unique laboratories for investigating the physics of dense and cold bulk nuclear matter, in which the strong force contributes to the pressure and exotic states might be present (for a review see, e.g., Lattimer & Prakash 2016; Watts et al. 2016). A key diagnostic of dense matter is its equation of state (EoS), i.e., the pressure-density relation. A variety of EoS have been proposed, each representing a different possible theory describing the properties of dense matter, which are still consistent with data from heavy-ion colliders and other experiments (see, e.g., Lattimer & Prakash 2016; Rezzolla et al. 2018). Based on them, the Tolman–Oppenheimer–Volkoff equations are integrated and present-day NS models and sequences are calculated for each EoS. The predicted macroscopic properties of NSs can be tested against astrophysical measurements and constraints. In particular if some key observables, chiefly NS masses, M, and radii, R, can be accurately measured, it is then possible to constrain the EoS. In fact different EoS predict different M–R relations: for example models based on GS1 (Glendenning & Schaffner-Bielich 1999) contain large amounts of exotic particles which "soften" the EoS, giving rise to relatively small radii and maximum masses; on the other hand, strange quark matter stars with low masses are almost incompressible (Lattimer & Prakash 2004). A variety of nucleonic NS models predict the radius to be nearly insensitive to the mass around $\sim 1 \div 1.5\ M_{\odot}$ (e.g., MPA1, MS2, AP3 as, respectively, Müther et al. 1987; Müller & Serot 1996; Akmal et al. 1998), which makes the determination of the radius of stars in that range a crucial factor in discerning among different EoS.

Two different approaches have been discussed in EoS testing. The direct approach consists in determining the likelihood that the measured M and R pairs match the M–R relation predicted by a given EoS. The other approach, pioneered by Lindblom (1992), involves the inverse process, namely mapping the measured M and R pairs to the EoS. Based on a parameterized representation of the EoS, Özel & Psaltis (2009) showed that several $\sim$5% precise measurements of M and R pairs are required to discriminate between EoS models with 3σ confidence.

Neutron star masses have been measured for a number of radio pulsars and X-ray binary systems (for a review, see Özel & Freire 2016) and, more recently, also in the merging NS binary GW 170817 (Abbott et al. 2018). The highest precision mass measurements are those from a few radio pulsar binaries containing two NSs (see, e.g., Burgay et al. 2003; Lyne et al. 2004).

Radii are far more difficult to measure; different techniques, mostly based on X-ray diagnostics, have been devised to determine either the NS radius itself or its ratio to the mass. X-ray spectroscopy-based techniques include (a) redshifted ion lines from the NS surface (if any, e.g., Cottam et al. 2002), (b) the flux and temperature of thermal emission from quiescent NS transients (e.g., Heinke et al. 2014) and (c) the evolution and "touch down" phase of thermonuclear flashes that give rise to photospheric radius expansion in accreting NSs (Lewin et al. 1993); the latter method provides simultaneous mass and radius measurements. Other possible techniques are based on timing diagnostics (see, e.g., Bhattacharyya 2010; Watts et al. 2016).

For instance, (d) the fastest NS spin periods (e.g., Haensel et al. 2009), as well as (e) the fastest quasi-periodic oscillation signals observed in X-ray binaries (if arising from Keplerian motion: see, e.g., Bhattacharyya 2010, Section 3.3.2 and references therein) provide mass-dependent upper limits on the radius which allow us to exclude entire regions of the M–R diagram; (f) the quasi-periodic X-ray signals observed during giant flares of magnetars, if asteroseismic in origin, hold the potential to measure both M and R (Israel et al. 2005; Steiner & Watts 2009); (g) a promising timing technique for simultaneous measurements of M and R exploits the X-ray modulation generated by hotspots on the surface of isolated or accreting NSs spinning with periods in the millisecond range (e.g., Nättilä & Pihajoki 2018). Most recently, this last method has been used on NICER observations of PSR J0030+0451 to constrain simultaneously its mass and radius to, respectively, ∼10% and ∼9% accuracy (Miller et al. 2019; Riley et al. 2019).

Along with these techniques, entirely different ones have been proposed to constrain the EoS of ultradense matter in NSs: (h) the measurement of a star's moment of inertia in relativistic radio pulsar binaries hosting two NSs, especially PSR J0737-3039A/B (Lattimer & Schutz 2005; Kehl et al. 2018); (i) the study of the tidal deformability in the merging events of two NSs through their gravitational wave signal (Hinderer et al. 2010; Raithel et al. 2018); (j) the analysis of the peak frequency of the post-merging gravitational wave signal, if a hypermassive, differentially rotating NS is formed in the merging events (Chatziioannou et al. 2017).

Despite considerable progress in recent years, radius (or combined mass and radius) measurements have not yet attained the required level of accuracy and precision to univocally determine the EoS (e.g., Watts et al. 2019). Limitations involve systematics, insufficient signal-to-noise or resolution, modeling uncertainties and scarcity of suitable systems or events.

In this paper we introduce a new X-ray spectroscopic technique aimed at determining the radius-to-mass ratio of NSs accreting through a disk in low-mass X-ray binaries (LMXBs). The technique exploits the very broad and redshifted profile of the Fe Kα line around 6 keV that is observed from a number of NS and stellar-mass black hole LMXBs, as well as AGNs. There exists by now a large body of evidence that these lines originate in the innermost disk regions, where their profile is determined by relativistic beaming, time dilation, red/blue-shifts, light bending, and frame dragging of matter orbiting the inner regions of accretion disks at nonnegligible fractions of the speed of light, c (Fabian et al. 1989; Reynolds & Nowak 2003; Reynolds 2014). The inner radius of the accretion disk is one of the key parameters that is routinely derived from combined fits to the Fe Kα profile and X-ray spectral continuum; in application to accreting NS systems inner disk radii as low as $\sim 6 \div 7\ GM/c^2$ were obtained in some cases, which provide upper limits on the star's radius-to-mass ratio (Bhattacharyya 2011). For example, by assuming a canonical NS mass of $1.4\ M_\odot$, Miller et al. (2013) found a maximum value of $R_{\rm NS} = 12.6$ km for Ser X-1 if the disk extended to the innermost stable circular orbit (ISCO) at $6\ GM/c^2$; similar values were inferred by applying the same reasoning to a few other LMXBs (Ludlam et al. 2017).

Our new technique applies to LMXBs seen under high inclinations ($i \gtrsim 65°$) in which the line-emitting disk extends to very close to the NS surface; in those systems we expect the body of the NS to occult the line flux from that part of disk innermost region that is behind the NS, giving rise to distinctive features in the Fe Kα line profile, which encode precise information on the R/M ratio.

Our paper is structured as follows: in Section 2 we describe our model and its approximations; in Section 3 we discuss the effects of occultation on different line profiles; Section 4 presents the first application of our technique to fit the X-ray spectrum of an NS LMXB system, 4U 1636-53, as determined from an observation with the Nuclear Spectroscopic Telescope Array (NuSTAR) satellite; we also investigate the precision of the radius-to-mass ratio measurements that can be obtained with large-area X-ray instruments of the next generation, in light of the extensive simulations we carried out; in Section 5 we discuss the limitations of our technique and outline future perspectives.

2. Line Profile Calculation

Our technique adopts a general relativistic approach in the Schwarzschild metric, exploits a high-precision approximation of strong-field photon deflection in the Schwarzschild spacetime and accounts for the angular dependence of the disk emissivity. The line flux measured by an observer at infinity at a given frequency $\nu_{\rm obs}$ is (Misner et al. 1973)

$$F_{\rm obs}(\nu_{\rm obs}) = \int \frac{I_{\nu_{\rm em}}}{(1+z)^3} d\Omega, \tag{1}$$

where $d\Omega$ is the solid angle subtended by the disk element in the observer's sky, $I_{\nu_{\rm em}}$ is the disk specific emissivity at the emission frequency, $(1+z)^{-1} = \nu_{\rm obs}/\nu_{\rm em}$ is the redshift factor and the integration extends over the whole disk surface contributing to the flux at $\nu_{\rm obs}$.

Equation (1) also includes information on the photon trajectories connecting emission points on the disk, here assumed to lie in the equatorial plane and have negligible vertical thickness ($\theta_{\rm em} = \pi/2$ for any emission point), to the observer. Photons emitted at $r_{\rm em}$ and $\varphi_{\rm em}$ travel along null geodesics lying on the plane defined by the lines connecting the origin to the emitting point and to the observer at infinity (the line of sight). We characterize these geodesics through the angle between the two aforementioned lines, ψ, and the angle between the emission direction and the radial direction, α (see Figure 1). Photon geodesics starting at $r_{\rm em}$ are described by (Chandrasekhar 1983; Beloborodov 2002)

$$\psi = \int_{r_{\rm em}}^{\infty} \left[\frac{1}{b^2} - \frac{1}{r^2}\left(1 - \frac{R_S}{r}\right)\right]^{-\frac{1}{2}} \frac{dr}{r^2}, \tag{2}$$

where b is the impact parameter of the photon trajectory and $R_S = 2GM/c^2$ represents the Schwarzschild radius. Throughout this paper we use geometric units ($G = c = 1$) and express lengths in units of the gravitational radius $GM/c^2 = r_g = R_S/2$. The impact parameter is related to α by

$$b = \frac{r_{\rm em} \sin\alpha}{\sqrt{1 - R_S/r_{\rm em}}} \tag{3}$$

and from spherical trigonometry we obtain

$$\cos\psi = \sin i \sin\theta \cos\varphi + \cos i \cos\theta. \tag{4}$$

A distinction must be made between photons with direct trajectories ($0 < \alpha < \pi/2$) and photons which go through a turning point ($\alpha > \pi/2$): the former always reach the observer, whereas those among the latter that reach infinity have impact

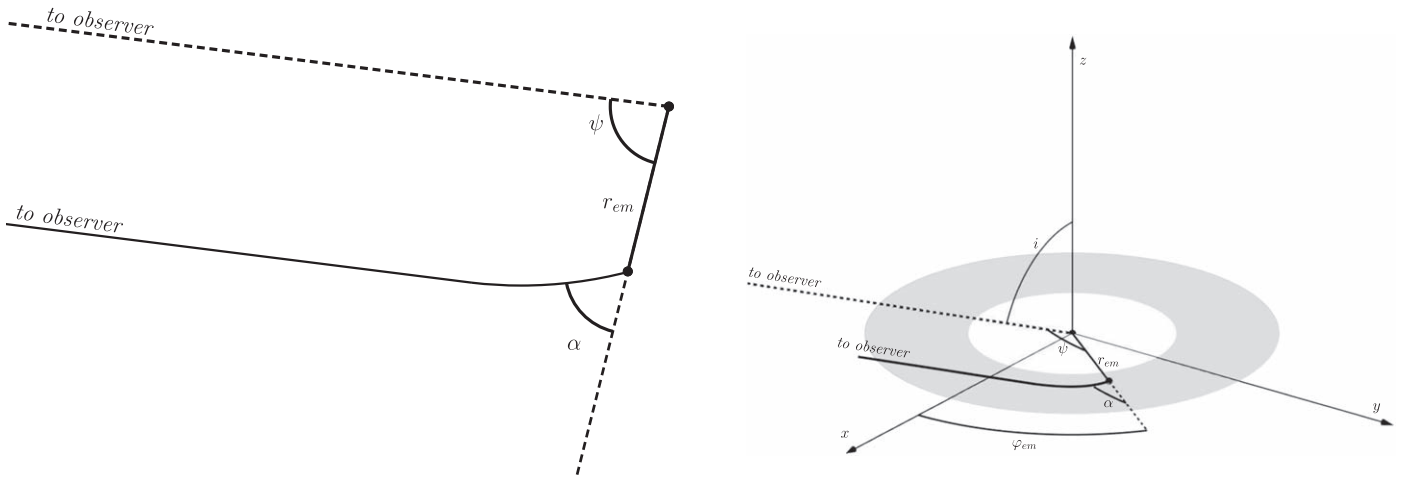

Figure 1. We show here a sample photon trajectory plane (left) and the geometry of our system (right): the observer, and thus the line of sight, lies on the xz plane while angles α and ψ lie on the photon trajectory plane, which also contains the line of sight. The inclination is denoted as i and the coordinates of the emitting point on the disk as $(r_{\rm em}, \varphi_{\rm em})$.

parameters $b > b_{\rm min} = 3\sqrt{3}\ r_g$ (Misner et al. 1973). This last condition translates into a limit on the maximum α angle through Equation (3); in Section 2.2 we discuss the way in which the above limit changes in the presence of a star whose radius exceeds $3\ r_g$.

Assuming that the disk matter moves along circular Keplerian orbits, the redshift factor of photons by any point on it is given by (e.g., De Falco et al. 2016)

$$(1+z)^{-1} = \frac{\sqrt{1-3r_g/r_{\rm em}}}{1+\frac{b}{r_{\rm em}}\sqrt{\frac{r_g}{r_{\rm em}}}\frac{\sin(i)\sin(\varphi_{\rm em})}{\sin(\psi)}}. \quad (5)$$

The solid angle element in the observer's sky is given by (Bao et al. 1994; De Falco et al. 2016)

$$d\Omega = \frac{b\ db\ d\varphi'}{D^2} = \frac{b}{D^2}\frac{\partial\varphi'}{\partial\varphi}\frac{\partial b}{\partial r}drd\varphi, \quad (6)$$

where φ' is calculated in the observer's frame, D is the distance to the system and the Jacobian is calculated through the partial derivatives $\partial b/\partial\psi$ and $\partial\psi/\partial r$ by means of Equation (2); its explicit form is

$$d\Omega = \frac{\frac{b^2\cos i}{r_{\rm em}^2 D^2\sin^2\psi\ \cos\alpha}}{\int_{r_{\rm em}}^{\infty}\left[1-\frac{b^2}{r^2}\left(1-\frac{R_S}{r}\right)\right]^{-\frac{3}{2}}\frac{dr}{r^2}}drd\varphi. \quad (7)$$

The specific intensity emitted in the local corotating frame of the disk is written as

$$I_{\nu_{\rm em}} = \delta(\nu-\nu_{\rm em})\mathcal{R}(r_{\rm em})\mathcal{A}(\cos\lambda_{\rm em}), \quad (8)$$

where $\nu_{\rm em}$ is the laboratory frequency of the emitted photon.

The radial emissivity law, $\mathcal{R}(r_{\rm em})$ is determined by the source of illumination of the disk and is usually approximated by a power law $\mathcal{R}(r_{\rm em}) \propto (r_{\rm em})^q$, with q in the $(-3 \div -2)$ range. In the so-called lamp-post geometry, a point-like source placed along the z-axis above the compact object (see, e.g., Martocchia & Matt 1996), we have $q = -3$ for $r_{\rm em} \geqslant 10\ r_g$ and a somewhat flatter dependence at smaller radii. The radial emissivity can be approximated with a single $q \simeq -3$ power law (or a broken power law) also when the illuminating source is not point-like but extended, as in the case of a hot gas corona hovering above the inner parts of the disk or enshrouding the NS (Wilkins 2018). An illuminating equatorial bright belt on the NS surface, resulting from energy released in the boundary layer between the accretion disk and the star, would present instead a marked steepening in the emissivity law at the smallest radii $r_{\rm em} \leqslant 8\ r_g$ (see Figure 5 in Wilkins 2018).

The angular dependence $\mathcal{A}(\mu = \cos\lambda_{\rm em})$ of the local disk emissivity (here $\lambda_{\rm em}$ is the angle between the photon emission direction and the disk normal, as measured in the corotating reference frame) is determined by the physical processes governing the production of line photons. We consider three different cases: limb-darkened, isotropic, and limb-brightened emission, the latter being favored when fluorescent emission results from illumination by an external X-ray source.

The limb-darkening law is modeled after Chandrasekhar (1950) assuming a pure scattering atmosphere, and its most commonly used form is $\mathcal{A}(\mu) \propto 1 + 2.06\mu$ (Laor 1991): the conditions that would produce such an emissivity, however, are difficult to warrant at all disk radii (see, e.g., Svoboda 2010, and references therein). Later works showed that a limb-brightening law would be more apt (Haardt 1993; Goosmann et al. 2007). This case is represented by an angular dependence $\mathcal{A}(\mu) \propto \log(1+1/\mu)$ (Haardt 1993), and it is also consistent with the results of Monte Carlo simulations of accreting systems (George & Fabian 1991; Matt et al. 1991; Ghisellini et al. 1994). Lastly, the law for isotropic emission $\mathcal{A}(\mu) =$ const. is more appropriate for low optical depths and no internal heating of the disk atmosphere (Fukue & Akizuki 2006), and can provide an intermediate case if the system configuration is poorly known, especially because the degree of ionization of the disk components is expected to play a role in the observed angular emissivity (see, e.g., Goosmann et al. 2007).

In Schwarzschild spacetime μ is given by (see, e.g., Chen & Eardley 1991; Bao et al. 1994)

$$\mu = \frac{b/r_{\rm em}}{(1+z)}\frac{\cos(i)}{\sqrt{1-\sin^2(i)\cos^2(\varphi_{\rm em})}} = \frac{\cos(i)\sqrt{1-3r_g/r_{\rm em}}}{\frac{\sin(\psi)}{\sin(\alpha)}\sqrt{1-\frac{2r_g}{r_{\rm em}}}+\frac{\sin(i)\sin(\varphi_{\rm em})}{\sqrt{r_{\rm em}/r_g}}}: \quad (9)$$

as expected, μ tends to $\cos(i)$ when $r_{\rm em} \to \infty$.

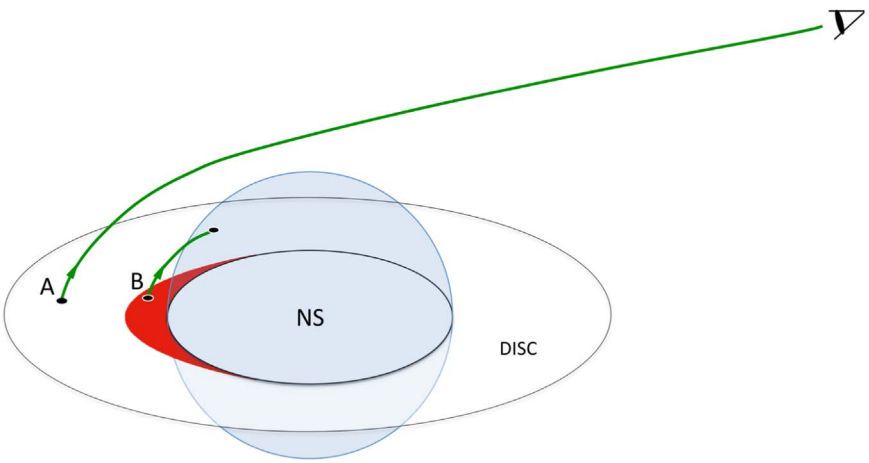

Figure 2. Simplified representation of the star body occulting part of the disk: photons starting from A reach the observer, whereas the ones emitted from the red "crescent" are intercepted by the star since their periastron falls beneath the star surface.

2.1. Analytical Approximation of the Photon Geodesic Equation

In order to avoid numerical integration of the photon geodesics, which would slow down the code considerably, we adopt an analytical approximation for Equation (2) (La Placa et al. 2019):

$$1 - \cos\alpha \approx (1 - \cos\psi)\left(1 - \frac{2r_g}{r}\right) \times \left[1 + k_1\frac{2r_g}{r}(1 - \cos(\psi - k_2))^{k_3}\right], \quad (10)$$

where $k_1 = 0.1416$, $k_2 = 1.196$, and $k_3 = 2.726$. This equation couples α to ψ and, together with Equations (3) and (4), it links the coordinates of an emitting point on the disk to the impact parameter.

The solid angle element (Equation (7)) can be approximated by using Equation (10) to calculate only the derivative $\partial b/\partial r$ (see, e.g., Bao et al. 1994), since the other terms in Equation (7) already are analytical.

2.2. Occultation

If the disk inner radius lies close to the surface of the star and the inclination under which we observe the system is high enough, some points on the far side of the disk ($x < 0$) will be occulted by the star itself notwithstanding the gravitational light bending.

The periastron for a given impact parameter b reads

$$p^2 - \left(1 - \frac{R_S}{p}\right)b^2 = 0 \quad (11)$$

and Equation (3) describes the relation between b and α, which in turn is connected to the coordinates on the disk through Equation (10): photon trajectories with a turning point whose periastron p falls under the star radius correspond to photons that are intercepted by the star and therefore do not reach the observer (Figure 2). Plugging Equation (3) into Equation (11) when taking $p = R_{\rm NS}$ determines the maximum accepted value of α, that indicates which region of the disk should be excluded from the integration of the line profile (Figure 3):

$$\alpha_{\max}(r_{\rm em}) = \pi - \arcsin\left[\frac{R_{\rm NS}}{r_{\rm em}}\sqrt{\frac{1 - R_S/r_{\rm em}}{1 - R_S/R_{\rm NS}}}\right]. \quad (12)$$

Figure 3 shows the shape and size of the occulted disk area behind the NS for different values of the inclination and the star radius: as expected, the occulted area increases for increasing inclinations and star radii.

We shall see that for high inclination and/or small inner disk radii the occultation of this crescent-like disk region by the body of the star imprints a characteristic feature on the line profile.

3. Partially Occulted Line Profiles

To calculate line profiles from the model described in Section 2 we wrote a Fortran subroutine, `shaddisk`, matching the specifications of the X-ray spectral fitting program XSPEC (Arnaud 1996). `shaddisk` carries out the integration over a grid of ($r_{\rm em}$, $\varphi_{\rm em}$) on the disk. The use of Equation (10) for the light bending and the solid angle element allows our code to run efficiently without resorting to numerical integration of photon geodesics or to interpolation of large matrices of precalculated values.

`shaddisk`'s parameters are the rest line energy E_o, the radial emissivity index q (assuming a power law $\mathcal{R}(r_{\rm em}) \propto (r_{\rm em}/r_g)^q$), the inner and outer radii, respectively $r_{\rm in}/r_g$ and $r_{\rm out}/r_g$, the inclination i, and the NS radius in units of the gravitational radius $R_{\rm NS}/r_g$. We note that this last parameter can also be thought of as the radius of an occulting sphere centered on the star, such as for instance a magnetosphere engulfed with matter of a Compton thick corona. Moreover, we inserted the possibility to choose among the three different angular emissivity laws discussed in Section 2.

The line profiles calculated with `shaddisk` in the case of absence of occultation were tested against the profiles from `kyrline` (Dovčiak et al. 2004) and `relline` (Dauser et al. 2010), setting the black hole spin to zero, for a range of parameters: excellent agreement was found in all cases.

To investigate the features of the occulted line model and the range of parameters over which they give rise to sizeable effects in the profile, we worked out a number of examples. We adopted a

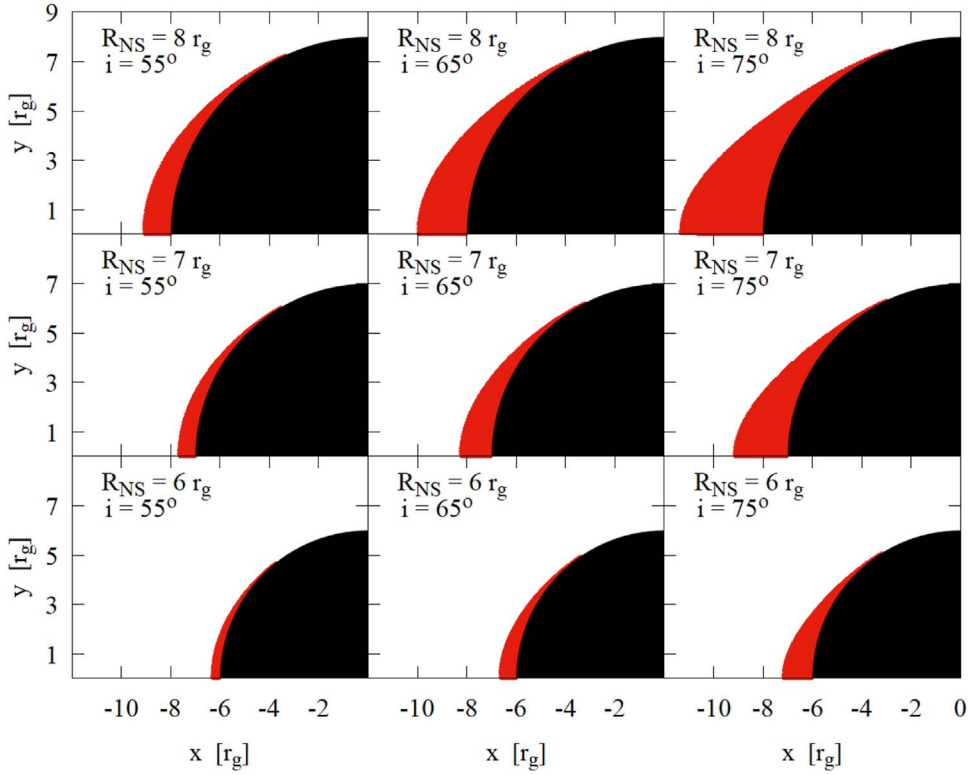

Figure 3. The nine panels show the extent of the occulted area (red) on disks that reach the NS (black), for different inclinations and star radii; the observers lie at infinity on the right, on the xz plane, so that the quadrants show half of the "back" side of the star relative to them ($90° \leqslant \varphi_{\rm em} \leqslant 180°$).

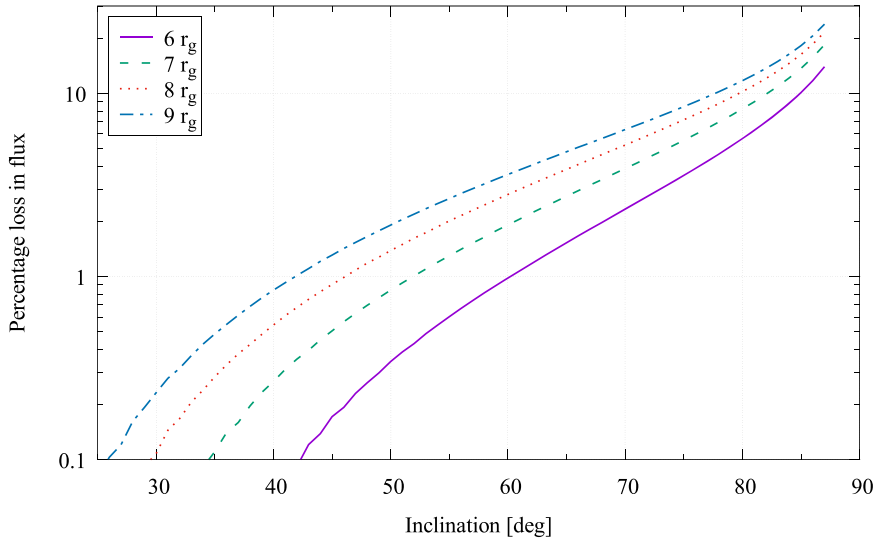

Figure 4. The percentage loss in total flux with respect to the unocculted case is plotted here for different star radii: we used $q = -3$ and the limb-brightening law, and the disk radii were set to $r_{\rm in} = R_{\rm NS}$, $r_{\rm out} = 5 \times 10^5\, r_g$.

limb-brightened surface emissivity and a radial power-law index of $q = -3$, comparing the disk line profile occulted by stars of different radii $\geqslant 6\, r_g$ with the unocculted case for which we set $R_{\rm NS} = 3\, r_g$ (note that any star with $R_{\rm NS} \lesssim 5\, r_g$ would produce no occultation features even for a 90° inclination).

The simplest consequence of the occultation of the inner part of the disk is a reduction in the observed flux. The degree to which occultation reduces the line flux relative to the unocculted case is plotted in Figure 4: values as high as 10% can be found for all star radii above 6 r_g when the disk reaches the star surface, and in all these cases a 2% reduction in flux is reached for $i < 70°$. Due to their higher relative flux in the central part of the disk, the isotropic and limb-darkening laws lead to enhanced emission from the far side of the inner disk regions, and thus to pronounced occultation features, compared with the limb-brightening case.

A mere line flux reduction, not accompanied by a change in the profile shape, would result simply in a lower equivalent width and thus remain undetectable in applications to real data. However, clear signatures emerge from a comparison between pairs of occulted and nonocculted line profiles. Four examples are shown in Figure 5 together with their difference and normalized ratio.

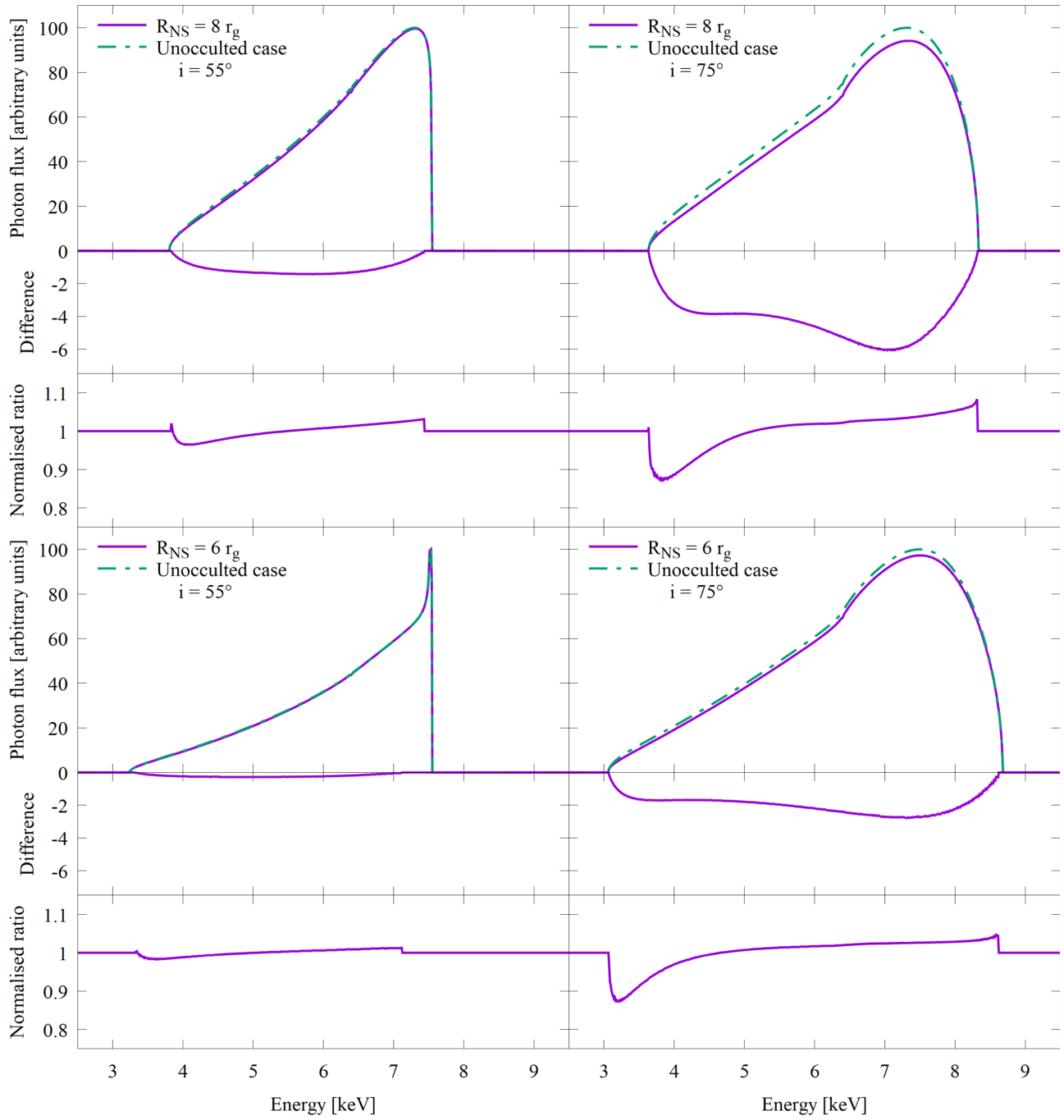

Figure 5. Occulted and unocculted line profiles for systems observed under an inclination of 55° and 75° (columns), hosting a central star of radius equal to 6 and 8 r_g (rows). In all cases, $r_{\rm in}$ is equal to the occulting star's radius, while $q = -3$, $r_{\rm out} = 5 \times 10^6\ r_g$, and the limb-brightening angular emission law was used. In each of the four subfigures the three panels show (top to bottom): (i) the occulted (solid) and unocculted (dotted–dashed) line profiles, with the flux expressed in units of the unocculted peak flux; (ii) the difference between the two profiles, in the same units as before; (iii) the ratio between the two profiles at each energy bin, normalized to its average value over the whole profile.

The shape of the normalized ratio displays a trough and peak close to the low and high energy ends of the profile, respectively: such asymmetry is due to the redshift distribution over the "crescent" of the far side of the disk that is occulted by the star. Since in systems observed under low inclinations or containing a small central star the most highly blueshifted photons are not occulted by the star surface, we see that in those profiles the highest energies are virtually unaffected (see, e.g., the bottom left subfigure in Figure 5, which represents a system with $R_{\rm NS} = 6\ r_g$ seen under $i = 55°$).

Occultation features scale, through Equation (12), as $R_{\rm NS}/r_g \propto R_{\rm NS}/M$: spectral analysis of occulted line profiles provides thus a new method to measure NS compactness.

4. Data Analysis and Simulations

Through the insertion of `shaddisk` into XSPEC as a local model (Arnaud et al. 2018), we used the partial occultation model as a tool to constrain or measure the $R_{\rm NS}/r_g$ ratio following two different approaches. In the first we analyzed the

spectrum from a high-inclination NS LMXB system, 4U 1636-53, as observed by the Nuclear Spectroscopic Telescope Array (NuSTAR; Harrison et al. 2013); in the second approach we simulated and analyzed X-ray spectra that could be obtained for the same system by next-generation instrumentation such as the Large Area Detector (LAD) on board the Enhanced X-ray Timing and Polarimetry mission (eXTP), currently under development and expected to launch in the mid-2020s (Zhang et al. 2019).

4.1. NuSTAR Analysis of 4U 1636-53

4U 1636-53 is a widely studied LMXB that has been observed in both the soft and hard states (Giacconi et al. 1974; Lyu et al. 2014, and references therein): its X-ray emission has a flux usually larger than 120 mCrab and shows a broad Fe Kα line, consistent with that produced by a disk extending close to the ISCO at 6 r_g (e.g., Ludlam et al. 2017).

The system displays thermonuclear (Type I) X-ray bursts during which a nearly coherent signal at 581 Hz arising from the NS rotation is frequently observed (Strohmayer et al. 1998). Its inclination is generally believed to be higher than 65°: certain estimates, including some based on the width of the Fe Kα line profile itself, return values of $i \gtrsim 80°$ (see, e.g., Pandel et al. 2008; Cackett et al. 2010; Lyu et al. 2014). However, this contrasts with the absence of dips or eclipses in the light curve from 4U 1636-53, which even allowing for favorable conditions in the system geometry seems to rule out inclination values higher than 75° (Sanna et al. 2013).

Ludlam et al. (2017) studied the X-ray spectrum of 4U 1636-53 from a 19.8 ks NuSTAR observation, looking in particular at the inner disk radius in order to set an upper limit on the NS radius-to-mass ratio. The instrumentation on board the NuSTAR mission boasts a 400 eV spectral resolution under 50 keV and is not affected by photon pile-up; it operates in the $3 \div 79$ keV band, with a peak in effective area of 800 cm^2 around 10 keV (Harrison et al. 2013). When taking the NS to be nonrotating, Ludlam et al. found best-fit values of $i = 76.5 \div 79.^{\circ}9$ and $r_{\rm in} = 6.00 \div 6.36\ r_g$, which suggests that occultation features in the iron line might be present, although small: therefore, we elected to analyze the same observation (ID 30101024002, 06/06/2015) within XSPEC.

In fitting the spectrum of 4U 1636-53 we added the partially occulted line profile model (`shaddisk`) to a relatively simple choice of components consisting of `diskbb` for the blackbody emission from the disk (see, e.g., Mitsuda et al. 1984); `pexriv` for the exponentially cutoff power-law spectrum reflected from the ionized material in and above the disk (Magdziarz & Zdziarski 1995); `kerrconv` for the relativistic smearing of the continuum spectrum (Brenneman & Reynolds 2006); `tbabs` for the absorption along the line of sight (Wilms et al. 2000).

Our fit results are summarized in Table 1: the reduced χ^2 is equal to $\chi^2/\#{\rm dof} = 1659/1490 = 1.113$, but the shape of the residuals suggests some missing contribution (see Figure 6). Let us note that the best-fit values for our main parameters of interest ($r_{\rm in}$, i, and $R_{\rm NS}$) are consistent at 90% confidence with the ones found in Ludlam et al. (2017), since we find $r_{\rm in} = 6.01^{+0.09}_{-0.01}\ r_g$, $i = 80.3^{+1.0}_{-0.6}$ degrees, and $R_{\rm NS} = 5.99^{+0.07}_{-5.99}\ r_g$, which clearly is just an upper limit on the NS radius.

The parameters derived from this analysis of 4U 1636-53 suggest that the signal-to-noise ratio provided by the current X-ray instrumentation is probably insufficient to measure the $R_{\rm NS}$ parameter with `shaddisk` in other high-inclination NS LMXB: we take, however, the continuum model components and values from Table 1 as the basis for our simulated eXTP observations of 4U 1636-53.

Table 1
Best-fit Values Using `tbabs`, `kerrconv`, `diskbb`, `pexriv`, and `shaddisk` on the NuSTAR Spectrum from 4U 1636-53

Component	Parameter	Units	Value	
TBabs	$n_{\rm H}$	10^{22} cm^{-2}	0.4	f
kerrconv	Index1	⋯	2.45	l
kerrconv	Index2	⋯	2.45	l
kerrconv	$r_{\rm br}$	(r_g)	150	f
kerrconv	a	⋯	0.0	f
kerrconv	Incl	deg	80.3	l
kerrconv	Rin	($r_{\rm ISCO}$)	1.0	l
kerrconv	Rout	($r_{\rm ISCO}$)	170	f
pexriv	PhoIndex	⋯	$1.772^{+0.004}_{-0.013}$	⋯
pexriv	foldE	keV	$19.26^{+0.14}_{-0.15}$	⋯
pexriv	rel$_{\rm refl}$	⋯	$0.34^{+0.05}_{-0.05}$	⋯
pexriv	Redshift	⋯	0.0	f
pexriv	abund	⋯	2.8	f
pexriv	Fe abund	⋯	2.8	f
pexriv	cosIncl	⋯	0.169	l
pexriv	$T_{\rm disk}$	K	1×10^6	f
pexriv	ξ	erg*cm s^{-1}	$2.9^{+2.1}_{-1.9} \times 10^3$	⋯
pexriv	norm	⋯	$0.404^{+0.001}_{-0.001}$	⋯
diskbb	Tin	keV	$0.53^{+0.02}_{-0.03}$	⋯
diskbb	norm	⋯	61.67	l
shaddisk	LineE	keV	$6.46^{+0.06}_{-0.22}$	
shaddisk	EmissInd	⋯	$-2.45^{+0.05}_{-0.05}$	⋯
shaddisk	Rin	(r_g)	$6.00^{+0.09}_{-0.00}$	⋯
shaddisk	Rout	(r_g)	990	f
shaddisk	Incl	deg	$80.3^{+1.0}_{-0.6}$	⋯
shaddisk	Rns	(r_g)	$5.99^{+0.09}_{-5.99}$	⋯
shaddisk	AngDep	⋯	−1.0 (limbbr.)	f
shaddisk	norm	⋯	$2.29^{+0.01}_{-0.01} \cdot 10^{-3}$	

Note. Parameter values indicated with f were fixed while the ones indicated with l were linked to other parameters. $n_{\rm H}$ is the equivalent column density of hydrogen on the line of sight used to calculate absorption; in `kerrconv` the two radial emissivity indices are both linked to `shaddisk`'s, so the break radius after which the routine uses the second one is fixed and irrelevant in this analysis, while the dimensionless spin a is fixed to 0 and the other parameters are linked to the relevant ones in `shaddisk`. The first two parameters in `pexriv` are the illuminating power-law photon index and cutoff energy, followed by rel$_{\rm refl}$ that defines what fraction of its emission is due to the reflected component, the system's redshift and the metal and iron abundances (in units of the solar ones); the cosine of the inclination is linked to i in `shaddisk` while $T_{\rm disk}$ and ξ are, respectively, the disk's temperature and ionization parameter. Lastly, `diskbb` only has the disk's temperature at the inner radius as a free parameter, since the normalization depends on the system's distance, inclination, and inner disk radius.

An extensive application of the new technique to archival X-ray spectra will be presented elsewhere. We did not attempt a similar analysis of 4U 1636-53 with the instrumentation on board XMM-Newton owing to the problems linked with it, such as dead time and photon pile-up.

4.2. Detecting the Occultation with Future Missions

The enhanced X-ray Timing and Polarimetry Mission (eXTP) is a Chinese-led mission being studied for a perspective

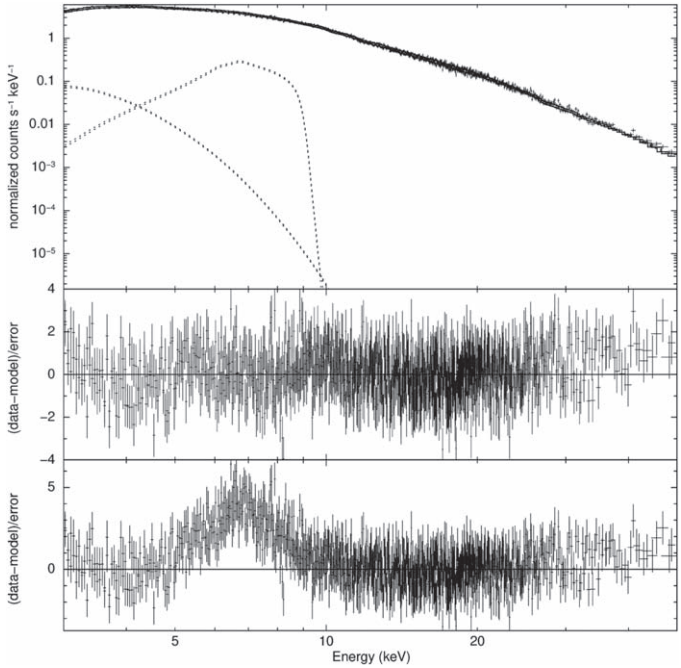

Figure 6. Best-fit NuSTAR spectrum of 4U 1636-53 obtained with the combination of `tbabs`, `kerrconv`, `diskbb`, `pexriv`, and `shaddisk`, and its residuals in the middle panel; the bottom panel shows the residuals when eliminating the iron line, i.e., accounting for the continuum alone.

launch in the mid-2020s (Zhang et al. 2019). Its main instrument, the LAD affords an effective area of 3.4 m^2 (about one order of magnitude larger than X-ray instruments of the past and present generations) in the $\sim 8 \div 10$ keV range and 1.5 m^2 at 2 keV, for a total range of $2 \div 80$ keV; it exploits large monolithic silicon drift detectors with a spectral resolution of $\sim$200 eV at 6 keV.

Through the use of its public response matrices, we simulated eXTP/LAD observations of 4U 1636-53 within XSPEC: for each simulation the integration time was set to 100 ks, while the energy range was constrained on the low end by the capabilities of eXTP: for the aims of this work we limited our spectra to the $2 \div 35$ keV range.

We generated spectra for three different star radii (6, 7, and 8 r_g), setting the inner disk radius first to the surface of the star and then one gravitational radius larger. The inclination was set to five different values for all disks that reached the star surface (60, 65, 70, 75, and 80°), then to 55° for the $R_{NS} = 8\ r_g$ case; when the disk is at 1 r_g from the surface, we considered at least three possible inclinations for each star radius, with more cases for larger stars. Thus, we produced and fitted a total of 28 different spectra, checking whether XSPEC could recover the initial parameter values of r_{in} and R_{NS} within a 90% confidence region.

The results are very promising: the contribution given by the occultation can be clearly singled out, as we can see from the residuals in the two middle panels in Figure 7 (compare with the middle panels in Figure 5).

Thanks to the high signal-to-noise ratio of large-area observations, the value of R_{NS} can be determined to precision within a few percent: Tables 2 and 3 summarize the best-fit values of the R_{NS} and r_{in} parameters for the various simulated spectra, together with their 90% confidence region. The actual star radius falls inside this 90% confidence range for every simulated spectrum except for the $R_{NS} = 7\ r_g$, $r_{in} = 7\ r_g$, $i = 75°$ case, whose 7 r_g value is slightly higher than the 6.96 r_g upper extremum of the confidence range.

Some clarifications are in order. First of all, the presence of some values whose lower limit is zero: in the case of the disk inner radius in systems with a 6 r_g star, this is due to 6 r_g already being the hard limit for the parameter, which makes it impossible for XSPEC to find a lower value. For the simulations with $R_{NS} = 6\ r_g$, $r_{in} = 7\ r_g$, and $R_{NS} = 7\ r_g$, $r_{in} = 8\ r_g$ instead, the difficulty in finding a lower limit on R_{NS} is given by the rather small (or absent) effect caused by the occultation: larger stars allow the right value of R_{NS} to be determined, as we can see from the $R_{NS} = 8\ r_g$, $r_{in} = 9\ r_g$ simulations.

In all except the aforementioned cases with $r_{in} = R_{NS} + 1\ r_g$, 90%-confidence errors on the NS radius are always under 5% of the R_{NS} value in either direction, the average being 2.2%; furthermore, most of them are below 3.5%. This is the precision expected to be necessary to put tight constraints on the EoS of supranuclear density matter based on NS parameters (Watts et al. 2019).

Moreover, we find that in all the simulations in which XSPEC only finds an upper limit on the star radius, this constraint is more stringent than the one imposed by the inner disk radius alone: this is true of both the cases with a 7 r_g and a 6 r_g star whose accretion disk does not touch the surface and it is another confirmation that the occultation effects (or in this case the lack thereof) can provide a strong limit on the radius-to-mass ratio. These results make us optimistic about the possibilities of future observations by large-area telescopes of both new and already observed systems to better constrain the R_{NS}/r_g ratio and therefore the EoS of NSs, hoping to shed more light on the behavior of ultradense matter.

5. Discussion and Future Perspectives

In this work we introduced a new technique to measure the radius-to-mass ratio of disk-accreting nonmagnetic NSs in X-ray binary systems by exploiting the features imprinted by occultation by the body of the star itself on the profile of the

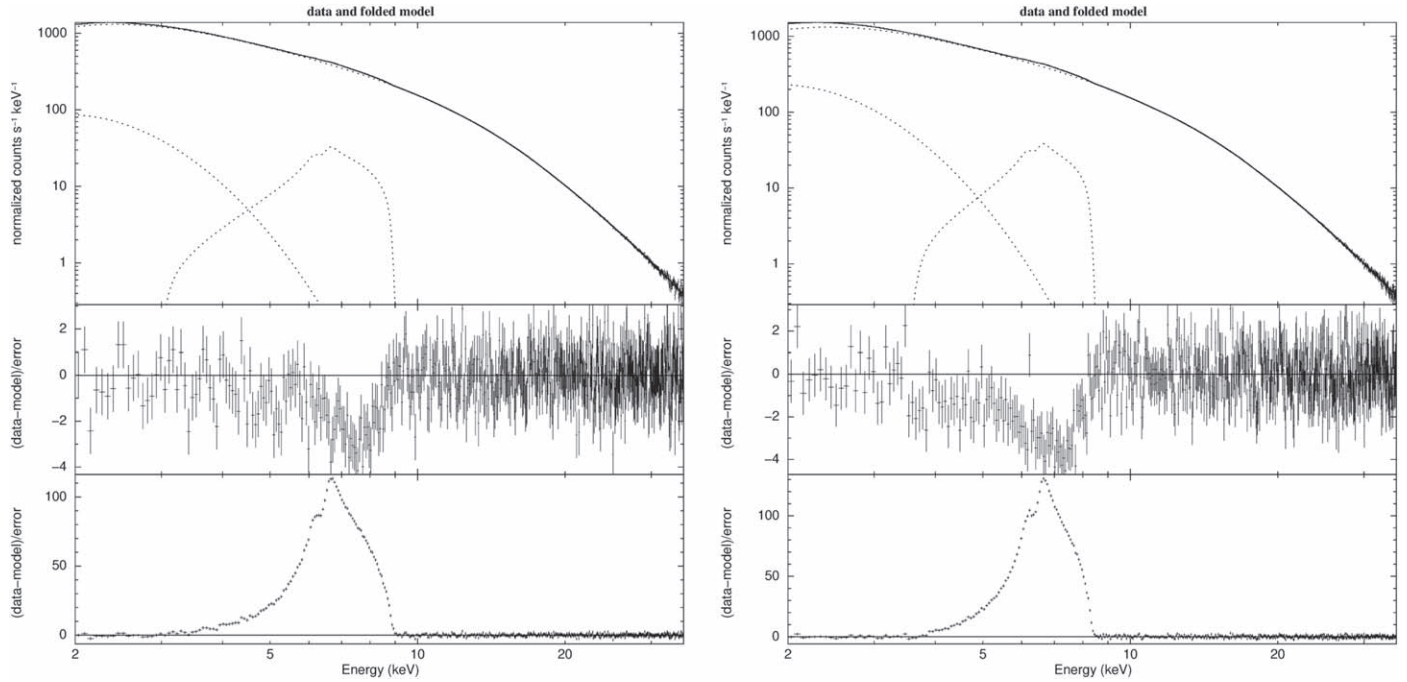

Figure 7. Simulated eXTP spectra from a 100 ks observation of a ∼120 mCrab system with (left) $R_{\rm NS} = 6\,r_g$, $r_{\rm in} = 6\,r_g$, and $i = 80^\circ$ and (right) $R_{\rm NS} = 8\,r_g$, $r_{\rm in} = 8\,r_g$, $i = 75^\circ$: in the two middle panels $R_{\rm NS}$ was set to $4\,r_g$, so the residuals correspond to the deviation produced by not accounting for the occultation; the bottom ones show the residuals with respect to the continuum alone, so that the missing iron line stands out clearly.

Table 2
Best-fit $r_{\rm in}$ and $R_{\rm NS}$ Parameters for the Simulations in which $r_{\rm in} = R_{\rm NS}$

	$R_{\rm NS} = 6\ r_g$		$R_{\rm NS} = 7\ r_g$		$R_{\rm NS} = 8\ r_g$	
i	$r_{\rm in}^{\rm bf}$	$R_{\rm NS}^{\rm bf}$	$r_{\rm in}^{\rm bf}$	$R_{\rm NS}^{\rm bf}$	$r_{\rm in}^{\rm bf}$	$R_{\rm NS}^{\rm bf}$
55°	…	…	…	…	$8.00^{+0.01}_{-0.02}$	$7.68^{+0.32}_{-0.21}$
60°	$6.00^{+0.01}_{-6.00}$	$5.90^{+0.11}_{-0.01}$	$7.01^{+0.01}_{-0.02}$	$6.85^{+0.16}_{-0.19}$	$8.00^{+0.01}_{-0.02}$	$8.00^{+0.01}_{-0.28}$
65°	$6.01^{+0.01}_{-0.01}$	$6.00^{+0.01}_{-0.23}$	$7.00^{+0.01}_{-0.01}$	$7.00^{+0.01}_{-0.15}$	$8.01^{+0.02}_{-0.01}$	$7.99^{+0.03}_{-0.30}$
70°	$6.00^{+0.02}_{-0.00}$	$5.96^{+0.04}_{-0.22}$	$7.00^{+0.01}_{-0.01}$	$7.00^{+0.02}_{-0.08}$	$8.00^{+0.02}_{-0.00}$	$7.88^{+0.17}_{-0.19}$
75°	$6.00^{+0.03}_{-6.00}$	$5.99^{+0.17}_{-0.13}$	$7.01^{+0.01}_{-0.03}$	$6.86^{+0.10}_{-0.15}$	$8.00^{+0.01}_{-0.04}$	$8.00^{+0.01}_{-0.10}$
80°	$6.00^{+0.01}_{-6.00}$	$5.94^{+0.06}_{-0.07}$	$6.99^{+0.03}_{-0.02}$	$6.98^{+0.16}_{-0.16}$	$8.00^{+0.03}_{-0.00}$	$7.99^{+0.02}_{-0.08}$

Table 3
Best-fit $r_{\rm in}$ and $R_{\rm NS}$ Parameters for the Simulations in which $r_{\rm in} = R_{\rm NS} + 1\ r_g$

	$R_{\rm NS} = 6\ r_g$		$R_{\rm NS} = 7\ r_g$		$R_{\rm NS} = 8\ r_g$	
i	$r_{\rm in}^{\rm bf}$	$R_{\rm NS}^{\rm bf}$	$r_{\rm in}^{\rm bf}$	$R_{\rm NS}^{\rm bf}$	$r_{\rm in}^{\rm bf}$	$R_{\rm NS}^{\rm bf}$
60°	…	…	…	…	$9.00^{+0.02}_{-0.03}$	$8.13^{+0.23}_{-0.34}$
65°	…	…	$8.00^{+0.02}_{-0.03}$	$7.07^{+0.31}_{-7.07}$	$8.95^{+0.01}_{-0.01}$	$8.15^{+0.24}_{-0.40}$
70°	$7.00^{+0.01}_{-0.01}$	$5.99^{+0.82}_{-5.99}$	$8.00^{+0.02}_{-0.01}$	$7.16^{+0.18}_{-0.20}$	$8.97^{+0.03}_{-0.01}$	$7.82^{+0.27}_{-0.23}$
75°	$6.99^{+0.02}_{-0.01}$	$5.99^{+0.36}_{-5.99}$	$8.05^{+0.03}_{-0.03}$	$7.12^{+0.22}_{-0.22}$	$8.91^{+0.04}_{-0.04}$	$7.87^{+0.28}_{-0.32}$
80°	$7.00^{+0.01}_{-0.01}$	$6.05^{+0.20}_{-0.15}$	$7.97^{+0.01}_{-0.01}$	$7.06^{+0.14}_{-0.16}$	$8.95^{+0.02}_{-0.02}$	$8.07^{+0.18}_{-0.18}$

relativistically broadened and redshifted Fe Kα originating from the disk. We developed a fast XSPEC routine (`shaddisk`) for the integration of the line profile that can be used efficiently to fit the X-ray spectra observed from these NSs.

We investigated the key characteristics of the technique, determining the conditions under which the trajectory of disk Fe Kα line photons intercepts the NS's surface, and calculated the Fe Kα line profiles for range of NS radii and disk inclinations, by using different prescriptions for the disk angular emissivity law. These profiles were compared with the corresponding unocculted ones, which allowed us to determine that occultation alters significantly the line profile for NS radii $\gtrsim 6 \div 7\ GM/c^2 \simeq 9 \div 10\ (M/M_\odot)$ km and disk inclinations $\gtrsim 65 \div 70^\circ$.

The analysis of the NuSTAR X-ray spectrum of the LMXB system 4U 1636-53 by using `shaddisk` did not provide statistically significant evidence that its Fe Kα line profile is affected by occultation by the NS body. Only an upper limit on

the star radius could be found, consistent with that derived from the inner disk radius ($\sim 6\, r_g$).

In order to check whether the occultation features can be detected in the Fe Kα line by very large effective area X-ray instruments of the next generation, we carried out extensive simulations by using the response matrices of the Large Area Detector, to be flown on board eXTP. The spectral parameters of 4U 1636-53 were used in these simulations, except that the line profile was varied over a range of disk inclinations and NS radii. The fit to the simulated spectra with `shaddisk` demonstrated that the occultation features can be revealed in the Fe Kα profiles over a wide range of parameters, resulting in $2 \div 3\%$ precise measurements of the NS radius-to-mass ratio in most cases ($\leqslant 5\%$ in all cases).

Some of the assumptions and limitations of our model are to be addressed: the occultation model that we developed implicitly assumes that the NS is nonrotating and spherical, and the innermost accretion disk region has negligible thickness. According to standard theory, the thickness-to-radius ratio h/R of the inner, radiation-pressure dominated region of the disk is of order $h/R \propto L/L_{\rm Edd} \sim 1\%$ for X-ray sources, like 4U 1636-53, whose luminosity is about 1% of the Eddington limit (Shakura & Sunyaev 1973). Therefore finite disk thickness will alter only to a very small extent the geometry of the occulted inner region of the disk.

Rotation induces oblateness, such that the occulting surface of the NS is that of an oblate spheroid, no longer that of a sphere. For the high end of the spin frequency distribution of accreting NSs ($\sim$600 Hz, as in the case of 4U 1636-53, Papitto et al. 2014; Patruno et al. 2017) the equatorial radius is about $5 \div 15\%$ larger than the polar radius, depending on the star's mass and EoS (see, e.g., Friedman et al. 1986; Morsink et al. 2007). The NS's oblateness will thus alter the outer border of the occulted inner disk "crescent" by making it slightly thinner in the middle and more elongated and thicker at the extremes: the Fe-line profiles will be slightly altered correspondingly. The rotation of the star (and the resulting oblateness) also alters the spacetime close to it with frame-dragging effects as well as terms arising from higher order mass multipoles: these in turn will affect matter and photon geodesics. However, these two effects have opposing contributions on both the position of the ISCO and the motion of the innermost disk regions (Morsink & Stella 1999; Bhattacharyya 2011): the Appendix provides approximate estimates of their impact, showing that for highly spinning NSs the analysis of partially occulted lines returns the value of the equatorial radius-to-mass ratio, which ensures that the technique would retain nearly the same level of accuracy even when applied to more realistic systems.

We conclude that the new method provides an innovative, independent way of measuring the radius-to-mass ratio of NSs with next-generation large-area X-ray instruments. Though limited to large enough NSs in binary systems seen from relatively high inclinations, the method will afford the few percent precision that is required to gather quantitative information on the EoS of matter at supranuclear densities (Watts et al. 2019); its precision is also comparable to that of other methods that will be exploited in the same time frame by using X-ray instrumentation of the same type, such as the eXTP/LAD. This is illustrated in Figure 8, where the constraint from our method intersects that from the two other techniques which exploit eXTP's instrumentation. It is apparent that the size of the allowed region would reduce considerably.

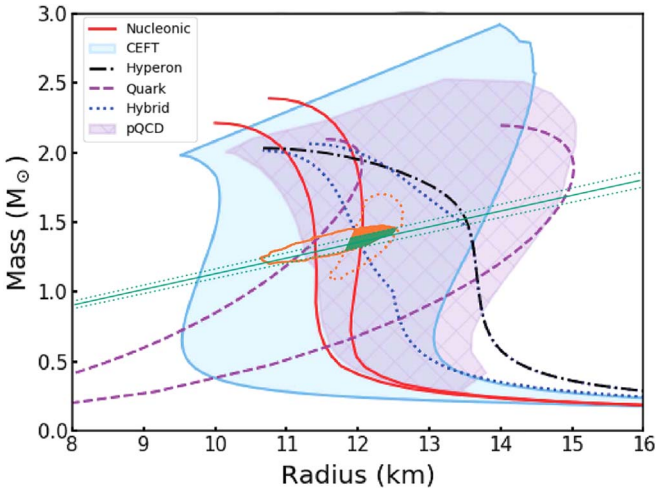

Figure 8. Limits on the mass–radius plane obtained with `shaddisk` if an $R_{\rm NS}/r_g$ ratio of 6 ± 0.18 is found (green lines): the errors correspond to 3% precision and are similar to the ones of the $R_{\rm NS} = 6\, r_g = r_{\rm in}$, $i = 75°$ simulation in Table 2. The underlying graph corresponds to a composition of Figures 3 and 7 in Watts et al. (2019), in which the open curves and areas indicated in the legend represent various equations of state, with different colors and styles for different underlying microphysics (for their description, see Watts et al. 2019). The orange solid curve (shifted down $\sim 0.1\, M_\odot$ for a clearer comparison) represents the kind of constraint we can obtain with eXTP from the modeling of the pulse profiles from localized hotspots on the star: when intersected with the confidence region that could be found through the analysis of atmosphere spectral models (orange dotted curve, also shifted down, Nättilä et al. 2017), this gives the filled area in orange. The simultaneous use of the three methods provides an even tighter constraint on the NS size (filled region in green).

We note that the model and code we developed can be employed also to search for Fe Kα partial occultation features originating from other bodies than the NS surface. For instance a spherical, optically thick corona such as that envisaged as the primary continuum X-ray source in models of disk-accreting compact objects would imprint features in the iron line that can be successfully singled out by the new technique. A detailed study of such systems will be presented in future works. Moreover, a convolution model based on `shaddisk` for the relativistic smearing and partial occultation of any spectral component has been recently finalized: this will extend the applicability of `shaddisk` to complex reflection models for disks around both NSs and black holes.

A.D.R., L.S., and T.D.S. acknowledge financial contribution from the agreement ASI-INAF n.2017-14-H.O. L.S. also acknowledges financial contributions from the ASI-INAF agreement I/037/12/0 and from the "iPeska" research grant (P.I. Andrea Possenti) funded under the INAF call PRIN-SKA/CTA (resolution 70/2016). A.P. acknowledges financial support from grants ASI/INAF I/037/12/0, ASI/INAF 2017-14-H.0 (PI: Belloni) and from INAF "Sostegno alla ricerca scientifica main streams dell'INAF," Presidential Decree 43/2018 (PI: Belloni).

Software: XSPEC (Arnaud 1996), HEAsoft (HEASARC Collaboration 2014), relline (Dauser et al. 2010), kyrline (Dovčiak et al. 2004), rns (Stergioulas & Friedman 1995), LSDplus (Bakala et al. 2015).

Appendix
Estimate of Smaller Effects on the Occulted Line Profiles

We investigate here the effects of the star's oblateness, rotation, and mass multipoles by comparing the line profiles obtained with `shaddisk` in the Schwarzschild metric to the ones produced by an advanced numerical code, *Lensing Simulation Device plus* (LSDplus; Bakala et al. 2015), starting by the simple case of an oblate star in the Schwarzschild metric. For a given equatorial radius, an oblate star occults less than a spherical one, and as expected we are able to observe more of the flux around the center of the broadened line profile, since matter in the area behind the NS moves almost perpendicularly to the line of sight. In particular, we considered an ellipticity $e = \sqrt{1 - R_{\rm pol}^2/R_{\rm eq}^2}$ of $e = 0.3$, corresponding to the rotational frequency $f = 600$ Hz using the empirical formula (see Equation (8) in Morsink et al. 2007) based on the modeling of NS structure through the *rns* code (Stergioulas & Friedman 1995): here, $R_{\rm pol}$ and $R_{\rm eq}$ are, respectively, the polar and equatorial radii of the star. Choosing the same X-ray continuum we used for the eXTP simulations, we generated the line profile occulted by the oblate star under LSDplus; the corresponding X-ray spectrum simulated with XSPEC features a disk going from the surface of the star ($R_{\rm eq} = 6\ r_g$) to $60\ r_g$, observed under an inclination $i = 70°$ for 100 ks by eXTP. Fitting this profile with `shaddisk` (which assumes the star to be spherical) we obtain a best-fit star radius of $5.70^{+0.12}_{-0.11}\ r_g$, which makes this case consistent with a slightly smaller star: in particular, since the polar radius of the oblate star is equal to $\sim 5.72\ r_g$, this best-fit value suggests that the occultation features on the line profile are more sensitive to the polar radius than to the equatorial one in the Schwarzschild metric.

For a second, more complete comparison, we needed to account for the influence the star rotation and oblateness have on the motion of disk matter. We adopted the formula for the Keplerian angular velocity on circular orbits in Hartle–Thorne geometry describing the external spacetime in the vicinity of a rotating NS. Recall that the Hartle–Thorne metric is a vacuum exact solution of the Einstein field equations that describes the exterior of any slowly and rigidly rotating, stationary and axially symmetric body. The metric is given with accuracy up to the second-order terms in the body's dimensionless angular momentum (spin) $j = J/M^2$, and first order in terms of its dimensionless quadrupole momentum, $q = -Q/M^3$ (see, e.g., Hartle & Thorne 1968; Abramowicz et al. 2003; Urbancová et al. 2019). The Keplerian angular velocity in the Hartle–Thorne geometry on the corotating circular geodesics with radius r is

$$\Omega_{\rm HT} = \Omega_{\rm K}(1 - j(r_g/r)^{3/2} + j^2\ F_1(r) + q\ F_2(r)), \qquad \text{(A1)}$$

where $\Omega_{\rm K}$ is the Keplerian angular velocity in the Schwarzschild geometry and the coefficients $F_1(r)$, $F_2(r)$ are given by Equations (17)–(20) in Abramowicz et al. (2003). The Hartle–Thorne angular velocity $\Omega_{\rm HT}$ increases with growing oblateness (i.e., increasing dimensionless quadrupole momentum q), but decreases with increasing spin j (for further details, see Urbancová et al. 2019).

The Kerr metric in the Boyer–Lindquist coordinates describing the stable rotating black hole corresponds the Hartle–Thorne metric after putting $q = j^2$ and applying a subtle coordinate transformation described by Equations (11) and (12) in Abramowicz et al. (2003). However, in the case of an NS the quadrupole momentum value is strongly related to the EOS of ultradense matter. Numerical modeling of NS structure shows that the value of dimensionless quadrupole momentum q can vary in the $(2 \div 12)j^2$ range and increases with growing stiffness of EOS (Arnett & Bowers 1977; Laarakkers & Poisson 1999; Morsink & Stella 1999). For an NS with mass $M = 1.4M_\odot$, rotational frequency $f = 600$ Hz and spin $j = 0.3$, we chose $q = 0.7$, close to the maximum dimensionless quadrupole moment (see Table 4 in Laarakkers & Poisson 1999). As with the previous case, we approximate the oblate shape of the NS with a spheroid characterized by an eccentricity $e = 0.3$ and $R_{\rm eq} = 6\ r_g$.

By generating another profile with LSDplus for this configuration and adding it to the usual continuum, we simulated another eXTP observation that we could fit with `shaddisk`. The resulting best-fit value of $R_{\rm NS} = 6.00^{+0.03}_{-0.12}\ r_g$ is consistent with the value of the equatorial radius owing to the interplay among frame-dragging effects, oblateness, and the additional contribution of the mass quadrupole (see also Bhattacharyya 2011, for similar results on the inner disk radius around rotating NSs). This consistency, although it introduces a degeneracy in discriminating between the rotating and nonrotating cases, ensures that the accuracy of this new method is essentially maintained when considering all the relevant effects.

Our tests and simulations to measure the value of $R_{\rm NS}/r_g$ were carried out by calculating the Fe Kα profile from a single ionization stage. In general, lines from multiple ionization stages might be emitted, possibly from different areas of the disk as first pointed out by Kallman & White (1989). The extent to which the overlap of two (or more) line profiles degrades the accuracy of the partial occultation model is hard to quantify. In principle one may associate different line emissions to radially distinct regions of the disk and carry out a fit in which only the innermost emission is potentially occulted. Alternatively, in the case of multiple ionization stages present over the whole disk, the convolution model of `shaddisk` could be used in conjunction with a suitable reflection model, such as `xillver` (García et al. 2013) or `reflionx` (Ross & Fabian 2005).

Nodal precession in the innermost regions of the accretion flow, as envisioned in a popular scenario for low frequency quasi-periodic oscillations (QPOs; Stella & Vietri 1998; Ingram & Done 2011), may also introduce uncertainties. Current modeling envisages that the illuminating inner hot corona or flow, rather than the inner disk, precesses, thus explaining the QPO-phase-resolved spectra with a varying, two-lobed illuminated area: the only source whose Fe Kα line has been analyzed through such a model to date is the black hole LMXB H 1743-322 (Ingram et al. 2017). Within such a frame, the possibility to produce occultation features is strongly linked to the radius at which this preceding corona truncates the disk: if the inner disk radius is close enough to the star surface, the analysis of the occultation features (or of their absence) can still yield a measurement or a tight upper limit on $R_{\rm NS}$ (see Section 4.2 and Table 3).

ORCID iDs

Riccardo La Placa https://orcid.org/0000-0003-2810-2394
Luigi Stella https://orcid.org/0000-0002-0018-1687
Alessandro Papitto https://orcid.org/0000-0001-6289-7413
Pavel Bakala https://orcid.org/0000-0003-0951-8597
Tiziana Di Salvo https://orcid.org/0000-0002-3220-6375
Maurizio Falanga https://orcid.org/0000-0003-3095-6065
Vittorio De Falco https://orcid.org/0000-0002-4728-1650
Alessandra De Rosa https://orcid.org/0000-0001-5668-6863

References

Abbott, B. P., Abbott, R., Abbott, T. D., et al. 2018, PhRvL, 121, 161101
Abramowicz, M. A., Almergren, G. J. E., Kluzniak, W., & Thampan, A. V. 2003, arXiv:gr-qc/0312070
Akmal, A., Pandharipande, V. R., & Ravenhall, D. G. 1998, PhRvC, 58, 1804
Arnaud, K., Gordon, C., & Dorman, B. 2018, An X-Ray Spectral Fitting Package (Greenbelt, MD: HEASARC), https://heasarc.nasa.gov/docs/xanadu/xspec/XspecManual.pdf
Arnaud, K. A. 1996, in ASP Conf. Ser. 101, Astronomical Data Analysis Software and Systems V, ed. G. H. Jacoby & J. Barnes (San Francisco, CA: ASP), 17
Arnett, W. D., & Bowers, R. L. 1977, ApJS, 33, 415
Bakala, P., Goluchová, K., Török, G., et al. 2015, A&A, 581, A35
Bao, G., Hadrava, P., & Ostgaard, E. 1994, ApJ, 435, 55
Beloborodov, A. M. 2002, ApJL, 566, L85
Bhattacharyya, S. 2010, AdSpR, 45, 949
Bhattacharyya, S. 2011, MNRAS, 415, 3247
Brenneman, L. W., & Reynolds, C. S. 2006, ApJ, 652, 1028
Burgay, M., D'Amico, N., Possenti, A., et al. 2003, Natur, 426, 531
Cackett, E. M., Miller, J. M., Ballantyne, D. R., et al. 2010, ApJ, 720, 205
Chandrasekhar, S. 1950, Radiative Transfer (Oxford: Clarendon Press)
Chandrasekhar, S. 1983, The Mathematical Theory of Black Holes (Oxford: Oxford Univ. Press)
Chatziioannou, K., Clark, J. A., Bauswein, A., et al. 2017, PhRvD, 96, 124035
Chen, K., & Eardley, D. M. 1991, ApJ, 382, 125
Cottam, J., Paerels, F., & Mendez, M. 2002, Natur, 420, 51
Dauser, T., Wilms, J., Reynolds, C. S., & Brenneman, L. W. 2010, MNRAS, 409, 1534
De Falco, V., Falanga, M., & Stella, L. 2016, A&A, 595, A38
Dovčiak, M., Karas, V., & Yaqoob, T. 2004, ApJS, 153, 205
Fabian, A. C., Rees, M. J., Stella, L., & White, N. E. 1989, MNRAS, 238, 729
Friedman, J. L., Ipser, J. R., & Parker, L. 1986, ApJ, 304, 115
Fukue, J., & Akizuki, C. 2006, PASJ, 58, 1039
García, J., Dauser, T., Reynolds, C. S., et al. 2013, ApJ, 768, 146
George, I. M., & Fabian, A. C. 1991, MNRAS, 249, 352
Ghisellini, G., Haardt, F., & Matt, G. 1994, MNRAS, 267, 743
Giacconi, R., Murray, S., Gursky, H., et al. 1974, ApJS, 27, 37
Glendenning, N. K., & Schaffner-Bielich, J. 1999, PhRvC, 60, 025803
Goosmann, R. W., Mouchet, M., Czerny, B., et al. 2007, A&A, 475, 155
Haardt, F. 1993, ApJ, 413, 680
Haensel, P., Zdunik, J. L., Bejger, M., & Lattimer, J. M. 2009, A&A, 502, 605
Harrison, F. A., Craig, W. W., Christensen, F. E., et al. 2013, ApJ, 770, 103
Hartle, J. B., & Thorne, K. S. 1968, ApJ, 153, 807
HEASARC Collaboration 2014, HEAsoft: Unified Release of FTOOLS and XANADU v6.25, Astrophysics Source Code Libraty, ascl:1408.004
Heinke, C. O., Cohn, H. N., Lugger, P. M., et al. 2014, MNRAS, 444, 443
Hinderer, T., Lackey, B. D., Lang, R. N., & Read, J. S. 2010, PhRvD, 81, 123016
Ingram, A., & Done, C. 2011, MNRAS, 415, 2323
Ingram, A., van der Klis, M., Middleton, M., Altamirano, D., & Uttley, P. 2017, MNRAS, 464, 2979
Israel, G. L., Belloni, T., Stella, L., et al. 2005, ApJL, 628, L53
Kallman, T., & White, N. E. 1989, ApJ, 341, 955
Kehl, M. S., Wex, N., Kramer, M., & Liu, K. 2018, in Proc. 14th Marcel Grossman Meeting, Recent Developments in Theoretical and Experimental General Relativity, Astrophysics, and Relativistic Field Theories, ed. M. Bianchi, R. T. Jansen, & R. Ruffini (Singapore: World Scientific), 1860
La Placa, R., Bakala, P., Stella, L., & Falanga, M. 2019, RNAAS, 3, 99
Laarakkers, W. G., & Poisson, E. 1999, ApJ, 512, 282
Laor, A. 1991, ApJ, 376, 90
Lattimer, J. M., & Prakash, M. 2004, Sci, 304, 536
Lattimer, J. M., & Prakash, M. 2016, PhR, 621, 127
Lattimer, J. M., & Schutz, B. F. 2005, ApJ, 629, 979
Lewin, W. H. G., van Paradijs, J., & Taam, R. E. 1993, SSRv, 62, 223
Lindblom, L. 1992, ApJ, 398, 569
Ludlam, R. M., Miller, J. M., Bachetti, M., et al. 2017, ApJ, 836, 140
Lyne, A. G., Burgay, M., Kramer, M., et al. 2004, Sci, 303, 1153
Lyu, M., Méndez, M., Sanna, A., et al. 2014, MNRAS, 440, 1165
Magdziarz, P., & Zdziarski, A. A. 1995, MNRAS, 273, 837
Martocchia, A., & Matt, G. 1996, MNRAS, 282, L53
Matt, G., Perola, G. C., & Piro, L. 1991, A&A, 247, 25
Miller, J. M., Parker, M. L., Fuerst, F., et al. 2013, ApJL, 779, L2
Miller, M. C., Lamb, F. K., Dittmann, A. J., et al. 2019, ApJL, 887, L24
Misner, C. W., Thorne, K. S., & Wheeler, J. A. 1973, Gravitation (San Francisco, CA: W.H. Freeman and Co.)
Mitsuda, K., Inoue, H., Koyama, K., et al. 1984, PASJ, 36, 741
Morsink, S. M., Leahy, D. A., Cadeau, C., & Braga, J. 2007, ApJ, 663, 1244
Morsink, S. M., & Stella, L. 1999, ApJ, 513, 827
Müller, H., & Serot, B. D. 1996, NuPhA, 606, 508
Müther, H., Prakash, M., & Ainsworth, T. L. 1987, PhLB, 199, 469
Nättilä, J., Miller, M. C., Steiner, A. W., et al. 2017, A&A, 608, A31
Nättilä, J., & Pihajoki, P. 2018, A&A, 615, A50
Özel, F., & Freire, P. 2016, ARA&A, 54, 401
Özel, F., & Psaltis, D. 2009, PhRvD, 80, 103003
Pandel, D., Kaaret, P., & Corbel, S. 2008, ApJ, 688, 1288
Papitto, A., Torres, D. F., Rea, N., & Tauris, T. M. 2014, A&A, 566, A64
Patruno, A., Haskell, B., & Andersson, N. 2017, ApJ, 850, 106
Raithel, C. A., Özel, F., & Psaltis, D. 2018, ApJL, 857, L23
Reynolds, C. S. 2014, SSRv, 183, 277
Reynolds, C. S., & Nowak, M. A. 2003, PhR, 377, 389
Rezzolla, L., Pizzochero, P., Jones, D. I., Rea, N., & Vidaña, I. 2018, ASSL, 457
Riley, T. E., Watts, A. L., Bogdanov, S., et al. 2019, ApJL, 887, L21
Ross, R. R., & Fabian, A. C. 2005, MNRAS, 358, 211
Sanna, A., Hiemstra, B., Méndez, M., et al. 2013, MNRAS, 432, 1144
Shakura, N. I., & Sunyaev, R. A. 1973, A&A, 24, 337
Steiner, A. W., & Watts, A. L. 2009, PhRvL, 103, 181101
Stella, L., & Vietri, M. 1998, ApJL, 492, L59
Stergioulas, N., & Friedman, J. L. 1995, ApJ, 444, 306
Strohmayer, T. E., Zhang, W., Swank, J. H., White, N. E., & Lapidus, I. 1998, ApJL, 498, L135
Svoboda, J. 2010, PhD thesis, Charles Univ.
Urbancová, G., Urbanec, M., Török, G., et al. 2019, ApJ, 877, 66
Watts, A. L., Andersson, N., Chakrabarty, D., et al. 2016, RvMP, 88, 021001
Watts, A. L., Yu, W., Poutanen, J., et al. 2019, SCPMA, 62, 29503
Wilkins, D. R. 2018, MNRAS, 475, 748
Wilms, J., Allen, A., & McCray, R. 2000, ApJ, 542, 914
Zhang, S., Santangelo, A., Feroci, M., et al. 2019, SCPMA, 62, 29502